Fast Multispectral Fusion and High-Precision Interdetector Image Stitching of Agile Satellites Based on Velocity Vector Field

Jiamin Du, Xiubin Yang, Meili Zhou, Ziming Tu, Shaoen Wang, Xingyu Tang, Lijie Cao, and Xindong Zhao

***Abstract*—When the targets are distributed irregularly, it is of great significance to quickly acquire color images with a wide field by agile satellite. Attributed to the changing of the three-axis attitude and Earth's rotation, there are misalignment and distortion during the processing of imaging by agile satellite. It makes the fusion of interband images slower and the stitching of interdetector images poorer. In this article, a rigorous velocity vector field (VVF) model is established through tracing rays between the image and the object. It calculates the misalignment among the images of bands in each detector to align and fuse multispectral images. Based on the reference image selected by VVF, the fused images are stitched with the method of leveraging line-point consistency. Finally, both field and in-orbit experiments are conducted. The time of calculating misalignment in image fusion with VVF is 13.19% of the minimum time of the traditional registration algorithm. In image stitching, our RMSE values are 1.15, which is the smallest among the RMSE values of SIFT, SURF, and SPW. In preserving linear structure, compared with SPW, the values of E_{dis}, E_{err}, and E_{cross}, respectively, reduce 60%, 50%, and 50%. The results show that images of the agile satellite can be fast fused and precisely stitched using VVF while correcting distortion. The compensation strategy of the VVF provides a theoretical basis for the agile satellite in image fusion and stitching.**

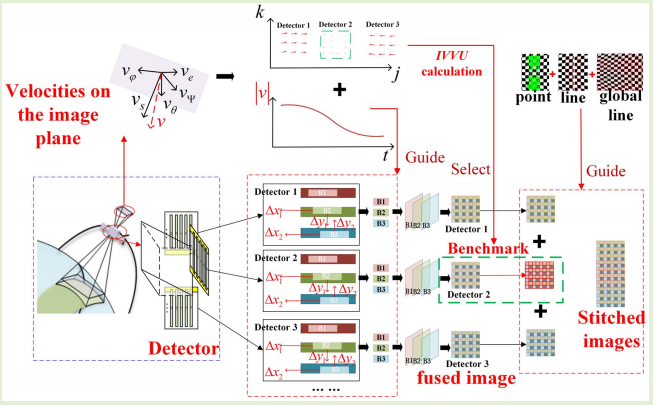

***Index Terms*— Agile satellite, fast multispectral images fusion, image stitching, spliced detector, velocity vector field (VVF).**

I. Introduction

NOWDAYS, remote sensing plays an important role in observing objects and obtaining information [1]. However, many objects with high economic value, such as cities along rivers, docks along coastlines, and oil–gas pipelines in meandering mountains, present an irregularly curvilinear distribution. The scanning traces of traditional space-based remote sensing are linear, which cannot meet the observation requirements [2], [3], [4]. To observe effectively, the satellite adjusts the agile attitude to cover all irregular distributed targets at a single scan [5]. Meanwhile, the image plane of agile satellites uses the optical method to splice several detectors, so as to enlarge coverage, such as Pleiades and ZY-3 [6], [7], [8]. It makes the images on one line to eliminate the shortcoming of asynchronous sampling, which is caused by temporal and spatial disparities of staggered spliced detectors in the traditional image plane. Each detector is affixed with several filters to obtain the multispectral information of the target, respectively. All filters are distributed in parallel to each other; each detector is independent of each other. It puts high demands on multispectral images fusion and interdetector image stitching. However, factors such as time-varying attitude angles, attitude angular velocities, Earth's rotation, and arrangement of detectors in agile satellite imaging can lead to severe misalignment and distortion, making it difficult for

Manuscript received 4 August 2022; revised 19 September 2022; accepted 22 September 2022. Date of publication 3 October 2022; date of current version 14 November 2022. This work was supported in part by the Natural Science Foundation of Jilin Province under Grant 20210101099JC, in part by the National Natural Science Foundation of China (NSFC) under Grant 62171430 and Grant 62101071, and in part by the Innovation and Entrepreneurship Team Project of Zhuhai City under Grant ZH0405190001PWC. The associate editor coordinating the review of this article and approving it for publication was Dr. Brajesh Kumar Kaushik. *(Corresponding author: Xiubin Yang.)*

Jiamin Du, Xiubin Yang, Meili Zhou, Ziming Tu, Shaoen Wang, and Xingyu Tang are with the Changchun Institute of Optics, Fine Mechanics and Physics, Chinese Academy of Sciences, Changchun 130033, China, with the University of Chinese Academy of Sciences, Beijing 100039, China, and also with Key Laboratory of Space-Based Dynamic & Rapid Optical Imaging Technology, Chinese Academy of Sciences, Changchun, Jilin 130033, China (e-mail: djm202028013920031@163.com; yangxiubin@ciomp.ac.cn; zhoumeili2011@126.com; sctzm@126.com; wangshaoen19961112@163.com; flashcomet@163.com).

Lijie Cao and Xindong Zhao are with the School of Remote Sensing and Information Engineering, Wuhan University, Wuhan, Hubei 430079, China (e-mail: cao2323756821@163.com; 2018302130101@whu.edu.cn).

Digital Object Identifier 10.1109/JSEN.2022.3209681

1558-1748 © 2022 IEEE. Personal use is permitted, but republication/redistribution requires IEEE permission.
See https://www.ieee.org/publications/rights/index.html for more information.

Authorized licensed use limited to: Changchun Inst of Optics Fine Mechanics & Physics. Downloaded on February 07,2023 at 01:20:13 UTC from IEEE Xplore. Restrictions apply.

images' fast fusion and precise stitch [9], [10], [11], [12]. Therefore, it is essential to increase the speed and improve the accuracy of image processing by analyzing the motion characteristics of agile satellite images.

Value and direction of the velocity vector are two main motion characteristics of agile satellite images. In 2004, Wang et al. [11] raised a velocity vector model of image motion using the coordinate transformation method, which had been widely used in remote sensing. However, large amounts of calculations were unavoidable, and the operation was complex. Since then, this model had been continuously developed. For instance, Jiang et al. [13]used spherical triangles to simplify the solution; Xu et al. [14] improved the accuracy by tracing ray. Meanwhile, special image motion models had been gradually established for satellites with different modes, such as polar satellites [15] and circular scanning satellites [14]. Recently, image motion models had been applied to estimating satellite attitude and restoring the image. Tong et al. [16] and Simon et al. [17] employed images to detect the oscillation motion. In the same year, Perrier et al. [18] used the image motion among multispectral images to retrieve the dynamics of the satellite. In 2020, Wang et al. [19] used the image rotation model to restore blurred images. In 2021, Liu et al. [20] studied the relationship between the vibration and image distortion. In those traditional instantaneous image motion models, velocities were rarely charging with time and pixel position. Thus, those models were only applicable for push-broom satellites, not agile satellites. It was difficult to calculate the misalignment of the multispectral images.

Points' feature matching algorithms are used to align images in the traditional multispectral image fusion. The image registration algorithms determine the speed of image fusion. Thus, it is constantly being improved. In 2004, Lowe [21] proposed the scale-invariant feature transform (SIFT) algorithm, but there were complex calculations and slow processing speeds. In 2008, Bay et al. [22] introduced the speeded-up robust features (SURF) algorithm, which was faster than the SIFT algorithm. These two methods were mostly used in aerospace image processing. Based on the algorithms, a number of improved algorithms had emerged. Cheng et al. proposed GS-SIST [23] and PIFT [24] algorithms, which improved alignment accuracy in feature point matching of multispectral images. However, it took a long time to traverse the image to match feature points. Thus, it could not meet the demands of fast fusion of agile satellite images.

After the fusion of multispectral images on each detector, independent color images are needed to be stitched together. Huang et al. [25] raise the precision of the point feature matching algorithm to generate stitched images with seamless visual effects of the MS1-02 satellite. What is more, the line feature could be extracted by the line segment detector (LSD) algorithm proposed by von Gioi et al. [26]. The method of combining point and line features was rarely used in aerospace image processing. Otherwise, distortion correction was also important during image stitching. Wang et al. [27] raised a high-precision seamless stitching method based on the geometric calibration of the camera. Xu et al. [28] corrected the distortion of images of satellites with a large pitch angle through deep learning and resolution inversion. The two methods did not correct the distortion in the course of the image stitching. In 2019, Liao and Li [29] came up with the SPW algorithm that preserved the local linear structure in the process of image stitching. In 2021, Jia et al. [30] introduced the local and global linear structures into stitching images, which could better suppress the bending of straight lines. Moreover, those linear features were evaluated by several parameters in [30]. There is currently no related work that applies the method of preserving local and global linear structures to distortion correction during stitching images of the agile satellite.

In order to solve the mentioned problems, the velocity vector field (VVF) model is proposed to quickly fuse images. Then, the fused images are stitched by the VVF model and the point-line registration algorithm considering linear structure. The remainder of this article is organized as follows. In Section II, a time-varying VVF of the agile satellite is introduced through theoretical analysis. In Section III, on the basis of misalignment, which is calculated by the VVF model, multispectral images are quickly aligned and fused. The fused image that has minimum distortion is selected by image velocity vector uniformity (IVVU). Referring to the selected image, line-point consistency that can protect local and global linear structure to correct distortion is used to precisely stitch the fused images. In Section IV, the field experiments are carried out to verify the feasibility of our method. In the meantime, the results are given accordingly. In Section V, images of the agile satellite are fused and stitched by our method. In Section VI, conclusions are summarized.

II. Model of Time-Varying Velocity Field for Agile Satellite

Agile satellite adjusts roll, pitch, and yaw attitude to image the targets that have an S-shaped distribution in 3-D object space. The position and velocity of the object point (the object point and the pixel are conjugate) imaged by the same pixel are varying with time. As shown in Fig. 1, it is complex and inefficient to consider all the object velocities influenced by satellite attitude in 3-D object space. It is amazing to find that only one resultant velocity will be obtained in the 2-D plane if all object velocities, such as the relative velocity v_s of the object to the satellite, the Earth's rotation velocity v_e, the pitch angular velocity v_θ, the roll angular velocity v_φ, and the yaw angular velocity v_Ψ, are projected to image plane. The resultant velocity is changing regularly with time, whose spatial and temporal variation properties can be represented on the 2-D image plane. It can well explain the correspondence of images among bands and detectors. Thus, it is necessary to establish the VVF model of agile satellites to analyze the resultant velocity, which has spatial and temporal variation properties.

It is the crux of establishing the VVF model to figure out the relationship between image and object. Exact object positions are solved first from image to object through ray tracing and spherical trigonometry. Then, velocity vectors are reversely projected from object to image based on exact object positions. This process goes through several right-hand Cartesian coordinate systems, as shown in Fig. 2, which will be defined as follows.

Authorized licensed use limited to: Changchun Inst of Optics Fine Mechanics & Physics. Downloaded on February 07,2023 at 01:20:13 UTC from IEEE Xplore. Restrictions apply.

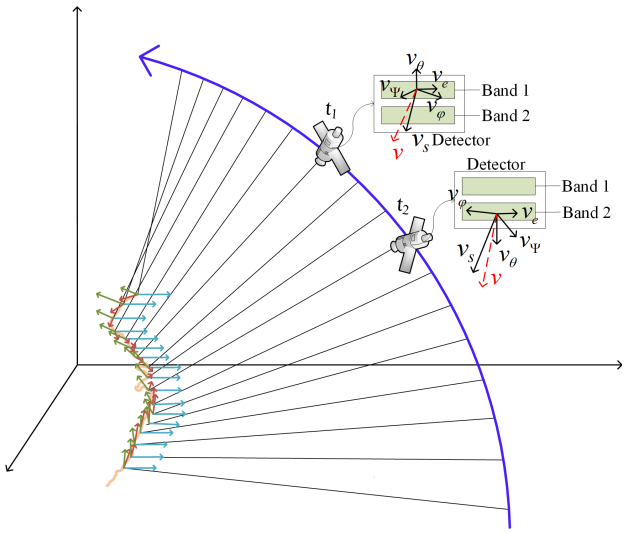

Fig. 1. Complex velocities in 3-D object space and their projected velocities on the 2-D image plane.

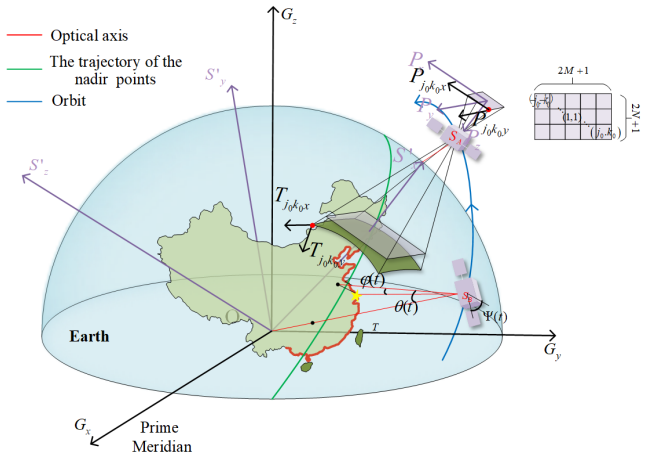

Fig. 2. Coordinate definition and attitude angles of the agile satellite.

1) *Earth Centered Fixed Coordinate System* $G(G_x, G_y, G_z)$*:* The origin is at the center of the Earth. It is fixed on the Earth and rotates with the Earth. The G_x-axis points to the intersection of the prime meridian and the Equator. G_z points to the North Pole.
2) *Geocentric Orbit Coordinate System* $S'(S'_x, S'_y, S'_z)$*:* The origin is at the center of the Earth. The S'_x-axis points to the satellite. The S'_z-axis is perpendicular to the orbital plane and coincides with the direction of angular momentum.
3) *Image Coordinate System* $P(P_x, P_y, P_z)$*:* The origin is at the center of image plane. The P_x-axis, on the detector plane, points to the direction of the satellite flight. The P_z-axis is parallel to the optical axis and points to the center of the Earth.
4) *Pixel Coordinate Systems* $P_{jk}(P_{jkx}, P_{jky})$*:* There are D pixels in the image plane, where $D = (2M+1)\times(2N+1)$. (j, k) represents the serial number of each pixel. The row number is $j \in (-M, M)$, and the column number is $k \in (-N, N)$. Thus, we can establish pixel coordinate systems P_{jk} whose amount is D. Their origins are at pixels (j, k) of the image plane. P_{jkx}-axes and P_{jky}-axes are on the image plane and parallel to the two edges of the image plane, respectively. The P_{jkx}-axis point to the direction of the satellite flight.
5) *Object Point Coordinate Systems* $T_{jk}(T_{jkx}, T_{jky})$*:* The series number (j, k) of each object point is the same as that of the pixel so that there are T_{jk} whose amount is D. Their origins are at object points. T_{jkx}-axes are tangential to the Earth's surface and point to the direction of satellite flight. T_{jkx}-axes are perpendicular to the T_{jky}-axes and tangential to the Earth's surface. Meanwhile, the T_{jky}-axis points in the direction of the Earth's rotation.

Coordinate systems P_{jk} and T_{jk} take the influence of the Earth's curvature into account, which improves the accuracy of the object–image projection. It should be emphasized that the following simplifications are reasonable during building the model: the geocentric point and centroid coincide; the geocentric latitude coincides with the geographic latitude.

A. Solution of Object Positions

The exact positions' calculation is the first step of building the VVF model. First, the angle relationship between pixels and objects is built through tracing rays. Then, the latitude of the nadir point is calculated through coordinate transformation. Finally, considering the angle relationship and the latitude of the nadir object, the latitudes of all object points are obtained by solving spherical triangles.

1) Angle Relationship Between Pixels and Objects Used in Building Model: In order to find out the positions of object points, three kinds of angles will be considered. They are satellite attitude angles, pixel angles, and geocentric angles.

1) *Satellite Attitude Angles:* The attitude angles and attitude angular velocities are considered first. The optical axis of satellite S_A without complex attitudes directs to the center of the Earth, which is shown in Fig. 2. During the flight of the agile satellite, it successively adjusts the pitch angle $\theta(t)$, pitch angle velocities $\dot{\theta}(t)$, roll angle $\varphi(t)$, and roll angle velocities $\dot{\varphi}(t)$ to ensure that the optical axis always points to the targets. At the same time, the satellite continuously adjusts the yaw angle $\Psi(t)$ and yaw angle velocities $\dot{\Psi}(t)$ to ensure that the image plane always scans along the direction of resultant velocity on the image plane.
2) *Pixel Angles:* Next, the pixel angles are introduced in detail based on yaw angles. The relationship between object and image is shown in Fig. 3(a). The pixel angles are α_{jk} and $\beta_{jk}(t)$. The focal length of the satellite is f, and the size of the pixel is a. The position of the pixel (j, k) in coordinate $P(P_x, P_y, P_z)$ can be always expressed as (xa, ya). The expressions for x and y are shown as follows:

$$x(t) = \mathrm{sgn}(j)\cdot j\cos\left(\gamma_{jk} - \Psi(t)\right) \quad (1)$$

$$y(t) = \mathrm{sgn}(j)\cdot k\sin\left(\gamma_{jk} - \Psi(t)\right) \quad (2)$$

$$\gamma_{jk} = \arctan\left(\frac{j}{k}\right). \quad (3)$$

Authorized licensed use limited to: Changchun Inst of Optics Fine Mechanics & Physics. Downloaded on February 07,2023 at 01:20:13 UTC from IEEE Xplore. Restrictions apply.

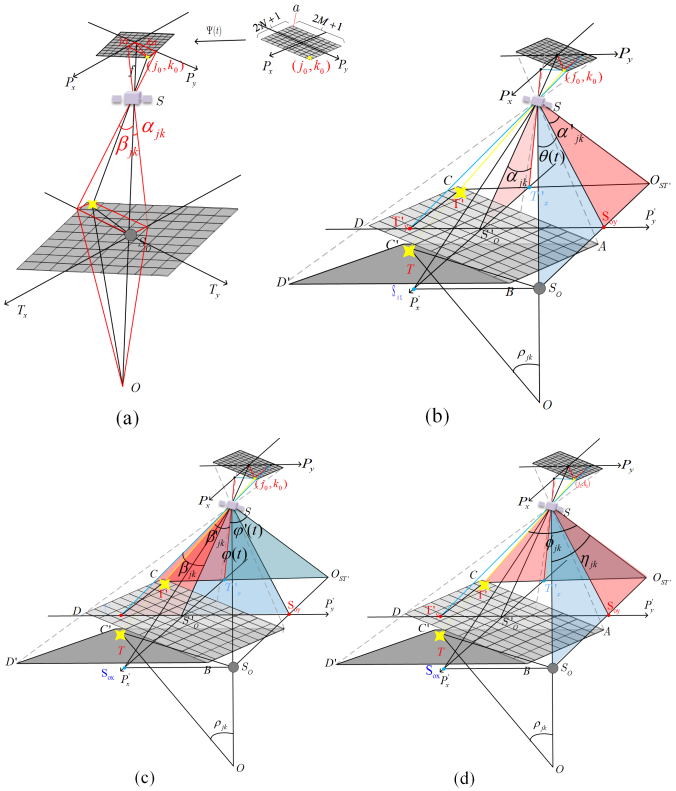

Fig. 3. Positional relationship and angle relationship between pixels (j, k) and their object points: (a) pixel angles $\alpha_{jk}(t)$ and $\beta_{jk}(t)$ when there is only yaw angle $\vartheta(t)$, (b) angle $\eta_{jk}(t)$ consisted of pixel angles $\alpha_{jk}(t)$ and pitch angle $\theta(t)$, (c) angle $\phi_{jk}(t)$ consisted of pixel angles $\beta_{jk}(t)$ and roll angle $\varphi(t)$, and (d) position determined by $\eta_{jk}(t)$ and $\phi_{jk}(t)$ in turn.

$\mathrm{sgn}(j)$ is the sign function

$$\mathrm{sgn}(j) = \begin{cases} 1, & j > 0 \\ 0, & j = 0 \\ -1, & j < 0. \end{cases} \tag{4}$$

The pixel angles of (j, k) in the direction of P_x and P_y can be described as $\alpha_{jk}(t)$ and $\beta_{jk}(t)$

$$\alpha_{jk}(t) = \arcsin\left(\frac{x(t)\cdot a}{\sqrt{(y(t)\cdot a)^2 + f^2}}\right) \tag{5}$$

$$\beta_{jk}(t) = \arcsin\left(\frac{y(t)\cdot a}{\sqrt{(x(t)\cdot a)^2 + f^2}}\right). \tag{6}$$

3) *Geocentric Angles:*
Finally, the geocentric angles are solved based on the pixel angles of each pixel and the attitude angles, which are illustrated in Fig. 3(b)–(d). The roll angle $\varphi(t)$ and the pitch angle $\theta(t)$ are first considered along with the yaw angle $\Psi(t)$. Red angles represent attitude angles and their relative projected angles. Blue angles represent the pixel angles of (j, k) and its relative projected angles. The projection of the image plane on the Earth is $A'B'C'D'$. $ABCD$, parallel to the image plane, is called the process plane. The origin S'_O is set at the center of $ABCD$. $P'_x \parallel P_x$, and $P'_y \parallel P_y$. S_O is the nadir point. T is the object point of pixel (j, k). There is a process target point T' on $ABCD$. S_{ox} and S_{oy} are the points acquired by projecting the nadir point S_o to the P'_x-axis and the P'_y-axis, respectively. T'_x and T'_y are the points acquired by projecting the process target point T' to the P'_x-axis and the P'_y-axis, respectively. SS'_0 is the optical axis. The extension lines of S_oS_{oy} and $T'T'_x$ intersect at point ST'.

Along the P'_x-axis, the pitch angel $\theta(t)$ and the pixel angle $\alpha_{jk}(t)$ are marked in Fig. 3(b). There are $\angle S_OSS_{Oy} = \theta(t)$ and $\angle S'_oSS_{oy} = \varphi(t)$. $\angle S_{oy}SO_{ST'_x} = \alpha'_{jk}(t)$ is projected by angle $\angle S'_OST'_x = \alpha_{jk}(t)$. It can also be known that $\angle S_oSO_{ST'} = \theta(t) + \alpha'_{jk}(t)$, which can be solved by (7)–(9). $\eta_{jk}(t)$ is used to represent $\angle S_oSO_{ST'}$. According to the principle of ray tracing, S_o will coincide with $O_{ST'}$ when SS_O rotates with angle $\eta_{jk}(t)$ along $S_{oy}O_{ST'}$

$$\begin{aligned}\eta_{jk}(t) &= \theta(t) + \alpha'_{jk}(t) \\ &= \arctan\left(\cos\frac{\tan\left(\alpha_{jk}(t) + \theta'(t)\right)}{\varphi'(t)}\right)\end{aligned} \tag{7}$$

where $\varphi'(t)$ and $\theta'(t)$ are

$$\varphi'(t) = \arctan\left(\frac{\tan(\varphi(t))}{\cos(\theta(t))}\right) \tag{8}$$

$$\theta'(t) = \arctan\left(\tan(\theta(t))\cdot\cos\left(\varphi'(t)\right)\right). \tag{9}$$

Along the P'_y-axis, the roll angel $\varphi(t)$ and the pixel angle $\beta_{jk}(t)$ are considered in Fig. 3(c). It can be known that $\angle T'ST'_x = \beta'_{jk}(t)$ is the projected angle of $\angle S_OST'_y = \beta_{jk}(t)$, and $\angle O_{ST'}ST'_x = \varphi''(t)$ is the projected angle of $\angle S'_OSS_{oy} = \varphi(t)$. There is $\angle T'SO_{ST'} = \varphi''(t) + \beta'_{jk}(t)$, which is calculated by (10). $\phi_{jk}(t)$ is used to represent $\angle T'SO_{ST'}$. $O_{ST'}$ will coincide with T' when $SO_{ST'}$ rotates with angle $\phi_{jk}(t)$ along $O_{ST'}T'$

$$\begin{aligned}\phi_{jk}(t) &= \varphi''(t) + \beta'_{jk}(t) \\ &= \arctan\left(\frac{\tan\left(\beta_{jk}(t) + \varphi(t)\right)\cdot\cos\left(\eta_{jk}(t)\right)}{\cos(\theta(t))}\right).\end{aligned} \tag{10}$$

In general, SS_0 will coincide with ST' when SS_0 successively rotates with $\eta_{jk}(t)$ and $\phi_{jk}(t)$. There are $\eta_{jk}(t) = \theta(t) + \alpha'_{jk}(t)$ and $\phi_{jk}(t) = \varphi''(t) + \beta'_{jk}(t)$, as shown in Fig. 3(d).

To clearly solve geocentric angles ρ_{jk}, $\rho_{xjk}(t)$ and $\rho_{yjk}(t)$, $\phi_{jk}(t)$ and $\eta_{jk}(t)$ of (j, k) are marked in the geocentric inertial coordinate system $G(G_x, G_y, G_z)$ in Fig. 4. T is the object point of (j, k). Trajectories of target and nadir point are parallel. TT' is perpendicular to the trajectory of the nadir point, which intersects at point T'. Thus, it is clear that $\angle T'SS_0 = \eta_{jk}(t)$ and $\angle TST' = \phi_{jk}(t)$. The nadir point S_O rolls with η_{jk} to reach point T' and then pitches with $\phi_{jk}(t)$ to reach point T. There is $\Phi_{jk}(t) = \angle S_OST$ calculated by the following equation:

$$\Phi_{jk}(t) = \arccos\left(\cos\left(\phi_{jk}(t)\right)\cdot\cos\left(\eta_{jk}\right)\right). \tag{11}$$

As shown in Fig. 4, the geocentric angles $\rho_{yjk}(t)$, $\rho_{jk}(t)$, and $\rho_{xjk}(t)$ will be calculated in rectangular pyramids

Authorized licensed use limited to: Changchun Inst of Optics Fine Mechanics & Physics. Downloaded on February 07,2023 at 01:20:13 UTC from IEEE Xplore. Restrictions apply.

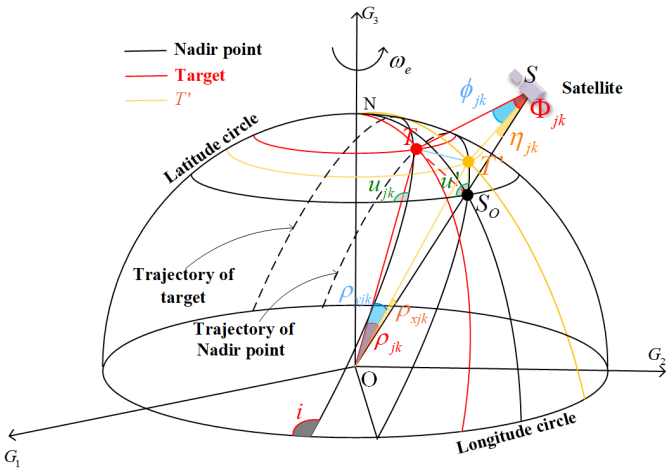

Fig. 4. Relationship between geocentric angles and attitude angles.

$S-TS_0T'$ and $O-TS_0T'$. R is the average radius of the Earth. The equations are

$$\rho_{jk}(t) = \arcsin\left[\frac{r\sin\left(\Phi_{jk}(t)\right)}{R}\right] - \Phi_{jk}(t) \tag{12}$$

$$\rho_{yjk}(t) = \arcsin\left[\frac{r\sin\left(\phi_{jk}(t)\right)}{R}\right] - \phi_{jk}(t) \tag{13}$$

$$\rho_{xjk}(t) = \arcsin\left[\frac{r\sin\left(\eta_{jk}(t)\right)}{R}\right] - \eta_{jk}(t). \tag{14}$$

The expressions of satellite attitude angles, pixel angles, and geocentric angles are finally obtained, which will be used in calculating the latitudes of objects of all pixels and solving VVF.

2) Latitude of Nadir Point: The latitude of the nadir point is the premise of the latitudes of other points. It can be expressed as $\delta_s(t)$

$$\delta_s(t) = \arcsin\left(\frac{z_s(t)}{\sqrt{(x_s(t))^2+(y_s(t))^2+(z_s(t))^2}}\right). \tag{15}$$

$(x_s(t), y_s(t), z_s(t))$ is the position of nadir point in $G(G_x, G_y, G_z)$, whose expression is (16). $E(t)$ means the eccentric anomaly of satellite

$$\begin{bmatrix} x_s(t) \\ y_s(t) \\ z_s(t) \end{bmatrix} = L_{S'G}\begin{bmatrix} r\cdot(1-e\cos(E(t))) \\ 0 \\ 0 \end{bmatrix}. \tag{16}$$

In (15), $L_{S'G}(t)$ represents the transformation matrix from the geocentric orbit coordinate system $S'(S'_x, S'_y, S'_z)$ to the Earth centered Earth fixed coordinate system $G(G_x, G_y, G_z)$

$$L_{S'G}(t) = \begin{bmatrix} \cos(\alpha_{G0}+\omega_e t) & \sin(\alpha_{G0}+\omega_e t) & 0 \\ -\sin(\alpha_{G0}+\omega_e t) & \cos(\alpha_{G0}+\omega_e t) & 0 \\ 0 & 0 & 1 \end{bmatrix} \times \begin{bmatrix} \cos(\omega+\theta_0) & \sin(\omega+\theta_0) & 0 \\ -\sin(\omega+\theta_0) & \cos(\omega+\theta_0) & 0 \\ 0 & 0 & 1 \end{bmatrix} \times \begin{bmatrix} 1 & 0 & 0 \\ 0 & \cos(i) & \sin(i) \\ 0 & -\sin(i) & \cos(i) \end{bmatrix} \times \begin{bmatrix} \cos(\mathrm{RAAN}) & \sin(\mathrm{RAAN}) & 0 \\ -\sin(\mathrm{RAAN}) & \cos(\mathrm{RAAN}) & 0 \\ 0 & 0 & 1 \end{bmatrix}. \tag{17}$$

α_{G0} is the Greenwich sidereal time at the epoch time. ω_e stands for the angular velocity of Earth's rotation. r means the semimajor axis of the satellite. e represents the eccentricity of the satellite orbit. i means the orbital inclination. RAAN is short for the right ascension of ascending node. ω is the argument of perigee. M_0 is the true perigee angle.

3) Latitudes of Objects of All Pixels: Considering the above relationship among pixels, objects, and the latitude of the nadir point, the exact latitudes of object points can be calculated.

As illustrated in Fig. 4, N is the North Pole. At time t, $\angle NS_0T' = u'(t) = \arccos(\cos i/\cos\delta_s)$ is the angle between the trajectory of nadir and latitude circle of nadir. $\angle TOT' = \rho_{yjk}(t)$ and $\angle T'OS_0 = \rho_{xjk}(t)$ are the geocentric angles.

The latitudes $\delta_{xjk}(t)$ of the object points that are influenced by pitch angle $\eta_{jk}(t)$ are calculated by solving the spherical triangle $\Delta NT'S_o$

$$\delta_{xjk}(t) = \arcsin\left[\sin(\delta_s(t))\cdot\cos\left(\rho_{xjk}(t)\right) \pm \cos(\delta_s(t))\cdot\sin\left(\rho_{xjk}(t)\right)\cdot\cos\left(u'(t)\right)\right]. \tag{18}$$

Then, the latitude $\delta_{jk}(t)$ of the object point is calculated by solving the spherical triangle ΔNTS_o

$$\delta_{jk}(t) = \arcsin\left[\sin\left(\delta_{xjk}(t)\right)\cdot\cos\left(\rho_{xjk}(t)\right) \pm \cos\left(\delta_{xjk}(t)\right)\cdot\sin\left(\rho_{xjk}(t)\right)\cdot\cos\left(u'(t)\right)\right]. \tag{19}$$

The signs of (18) and (19) are selected as follows: under the condition that the satellite is in the prograde orbit ($i < 90°$), when the latitude of the object point of the optical axis is higher than the latitude of the nadir point, "+" will be taken; otherwise, "−" will be taken. The selection rule for the signs is reversed when the satellite is in a retrograde orbit ($i > 90°$).

B. Velocity Vector Field

Based on the positions of object points, the exact VVF model can be established. As illustrated in Fig. 5, velocity vectors of each object point are decomposed on coordinate T_{jk}. Then, the decomposed velocities are projected to coordinate P_{jk} by the transformation matrix from coordinate T_{jk} to coordinate P_{jk}. Finally, the velocities of the yaw angular adjustment are added to the velocities on coordinate P_{jk}.

1) Velocity Vectors of Objects on T_{jk}: According to the latitudes, attitude angles, and geocentric angles, the expressions of velocities are acquired in coordinate T_{jk}. As shown in Fig. 5, the relative velocity v_{sjk} of the object to the satellite, the Earth's rotation velocity v_{ejk}, the pitch angular velocity $v_{\theta jk}$, and the roll angular velocity $v_{\varphi jk}$ are shown as follows:

$$v_{sjk}(t) = \omega_s R\cos\left(\rho_{yjk}(t)\right) \tag{20}$$

$$v_{ejk}(t) = \omega_e R\cos\left(\delta_{jk}\right) \tag{21}$$

$$v_{\varphi jk}(t) = \dot{\varphi}(t) L_{jk}(t)\cos\left(\rho_{yjk}(t)+\varphi(t)\right) \tag{22}$$

$$v_{\theta jk}(t) = \dot{\theta}(t) L_{jk}(t)\cos\left(\rho_{xjk}(t)+\theta(t)\right). \tag{23}$$

Authorized licensed use limited to: Changchun Inst of Optics Fine Mechanics & Physics. Downloaded on February 07,2023 at 01:20:13 UTC from IEEE Xplore. Restrictions apply.

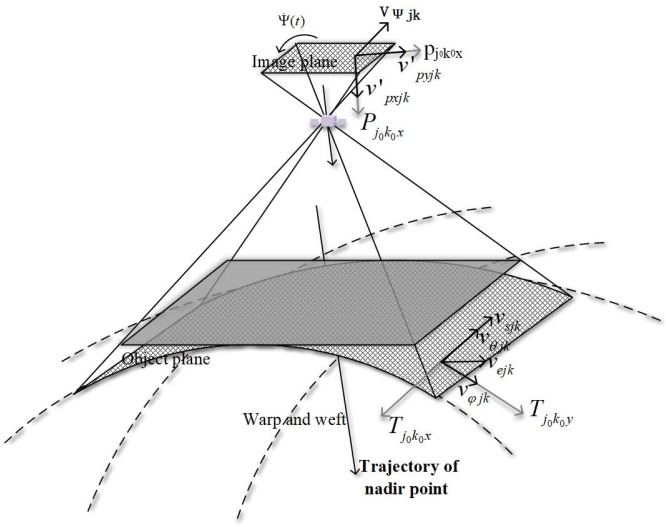

Fig. 5. Velocity vector on the object and image planes.

$L_{jk}(t)$ means the distance from the satellite to object points. The expression is

$$L_{jk}(t) = \sqrt{r^2 + R^2 - 2rR\cos\left(\rho_{jk}(t)\right)}. \tag{24}$$

As shown in Fig. 5, those velocities are decomposed in the coordinate system T_{jk}. The components, $v_{xjk}(t)$ and $v_{yjk}(t)$, along T_{xjk}- and T_{yjk}-axes can be viewed as follows:

$$v_{xjk}(t) = -v_{sjk}(t) - v_{ejk}(t)\cos\left(\pi - u_{jk}(t)\right) - v_{\theta jk}(t) \tag{25}$$

$$v_{yjk}(t) = v_{\varphi jk}(t) + v_{ejk}(t)\sin\left(\pi - u_{jk}(t)\right). \tag{26}$$

$u_{jk}(t)$ represents the angle between v_{sjk} and v_{ejk} at every object point

$$u_{jk}(t) = \arccos\left[\frac{\cos(i)}{\cos\left(\delta_{jk}(t)\right)}\right]. \tag{27}$$

2) Velocity Vectors Projection From Coordinate T_{jk} to Coordinate P_{jk}: The object velocities are projected to the image plane by the transformation matrix L_{TPjk}, which is from the coordinate system T_{jk} to coordinate system P_{jk}. The velocity components v'_{pxjk} and v'_{pyjk} on the image plane, as shown in Fig. 5, can be expressed as

$$\begin{bmatrix} v'_{pxjk}(t) \\ v'_{pyjk}(t) \\ 0 \end{bmatrix} = -L_{TPjk}(t)\begin{bmatrix} v_{xjk}(t) \\ v_{yjk}(t) \\ 0 \end{bmatrix}. \tag{28}$$

The expression for $L_{TPjk}(t)$ is given as follows:

$$L_{TPjk}(t) = \frac{f}{L(t)\cdot\cos\left(\alpha_{jk}(t)\right)\cdot\cos\left(\beta_{jk}(t)\right)} \times \begin{bmatrix} 1 & 0 & 0 \\ 0 & \cos\left(-\Phi_{jk}(t)\right) & \sin\left(-\Phi_{jk}(t)\right) \\ 0 & -\sin\left(-\Phi_{jk}(t)\right) & \cos\left(-\Phi_{jk}(t)\right) \end{bmatrix} \times \begin{bmatrix} 1 & 0 & 0 \\ 0 & \cos\left(-\rho_{jk}(t)\right) & \sin\left(-\rho_{jk}(t)\right) \\ 0 & -\sin\left(-\rho_{jk}(t)\right) & \cos\left(-\rho_{jk}(t)\right) \end{bmatrix}. \tag{29}$$

3) Resultant Velocity Vectors on Coordinate P_{jk}: Yaw angle velocities are introduced to coordinate P_{jk} to solve the value and direction of the resultant velocity vectors. The yaw angle adjustment is expressed as

$$v_{x\Psi jk}(t) = -\mathrm{sgn}(x)\cdot\dot{\Psi}(t)\cdot a\sqrt{(y)^2+(y)^2}\cdot\cos\left(\theta_{jk}\right) \tag{30}$$

$$v_{y\Psi jk}(t) = \mathrm{sgn}(x)\cdot\dot{\Psi}(t)\cdot a\sqrt{(x)^2+(y)^2}\cdot\sin\left(\theta_{jk}\right) \tag{31}$$

$$\theta_{jk} = \arctan\left(\frac{x}{y}\right). \tag{32}$$

The final expression of velocity on the image plane is

$$V_{pjk}(t) = \sqrt{V^2_{pxjk}(t) + V^2_{pyjk}(t)}. \tag{33}$$

There are

$$V_{pxjk}(t) = v'_{pxjk}(t) + v_{x\Psi jk}(t) \tag{34}$$

$$V_{pyjk}(t) = v'_{pyjk}(t) + v_{y\Psi jk}(t). \tag{35}$$

In (33), $V_{pjk}(t)$ is the value of the resultant velocity. Meanwhile, ξ is used to represent the direction of resultant velocity, which is called the drift angle

$$\xi = \arccos\left(V_{pxjk}(t)/V_{pjk}(t)\right). \tag{36}$$

III. Image Fusion and Stitching Method Using VVF Model

According to the VVF model of the agile satellite, velocities on the image plane vary with time and have anisotropic distribution. Meanwhile, the image plane of the agile satellite is spliced with several detectors that have a few parallel bands, whose imaging effect will be influenced by spatial and temporal distributions of VVF. Details of the image plane are shown in Fig. 6. The image plane is split into two planes by 45° reflective prism. The detectors are, respectively, arranged at intervals in those two planes. There is an overlapping imaging area between two adjacent detectors. At the same time, each detector has several multispectral bands, B1, B2, B3, and so on, with width S_p. They are parallelly arranged with interval S_h.

According to the distribution of B1, B2, B3, and so on, obvious misalignment of the multispectral images exists due to the image motion caused by time-varying velocity vectors. Meanwhile, the anisotropy of velocity vectors on the whole image plane leads to image distortion. The stitching of the images between detectors is inaccurate. Thus, the image fusion and stitching methods are proposed, as shown in Fig. 7.

A. Multispectral Images Fusion With VVF Model

The most important factor is feature alignment in multispectral image fusion. The speed of feature alignment determines the speed of image fusion. Thus, the velocity on the image plane is substituted into the kinematic equation to calculate the misalignment of the feature. According to the average principle, the time-varying velocity of the central pixel ($j = 0$, $k = 0$) of each detector is used to replace the time-varying velocity of the whole image plane since the anisotropy of the latter one has little effect on the fusion among bands.

Authorized licensed use limited to: Changchun Inst of Optics Fine Mechanics & Physics. Downloaded on February 07,2023 at 01:20:13 UTC from IEEE Xplore. Restrictions apply.

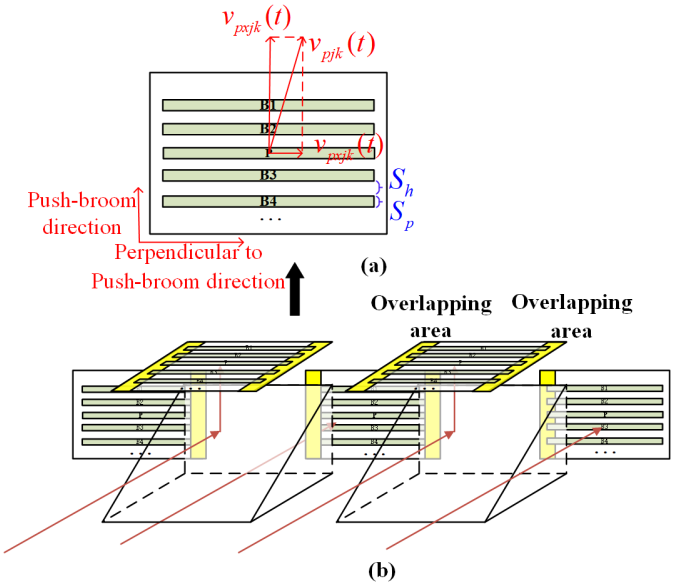

Fig. 6. Image plane spliced with several detectors by the optical method. (a) Velocities on each detector and relative parameters of the detector. (b) Arrangement of detectors.

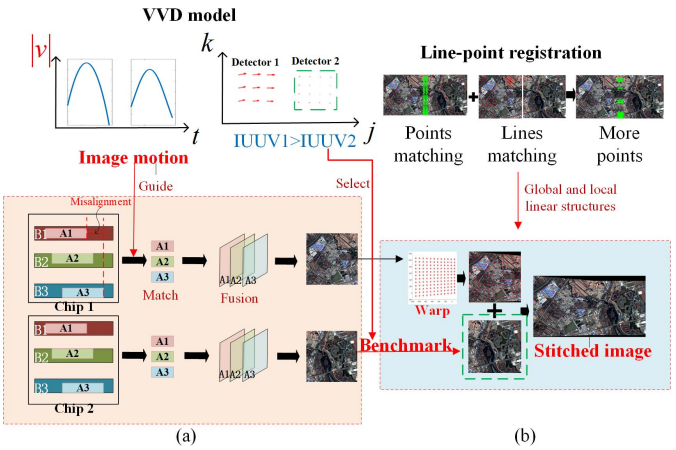

Fig. 7. Process of image fusing and stitching: (a) image fusion guided by VVF and (b) image stitching with distortion correction by the point-line registration method based on the selected benchmark.

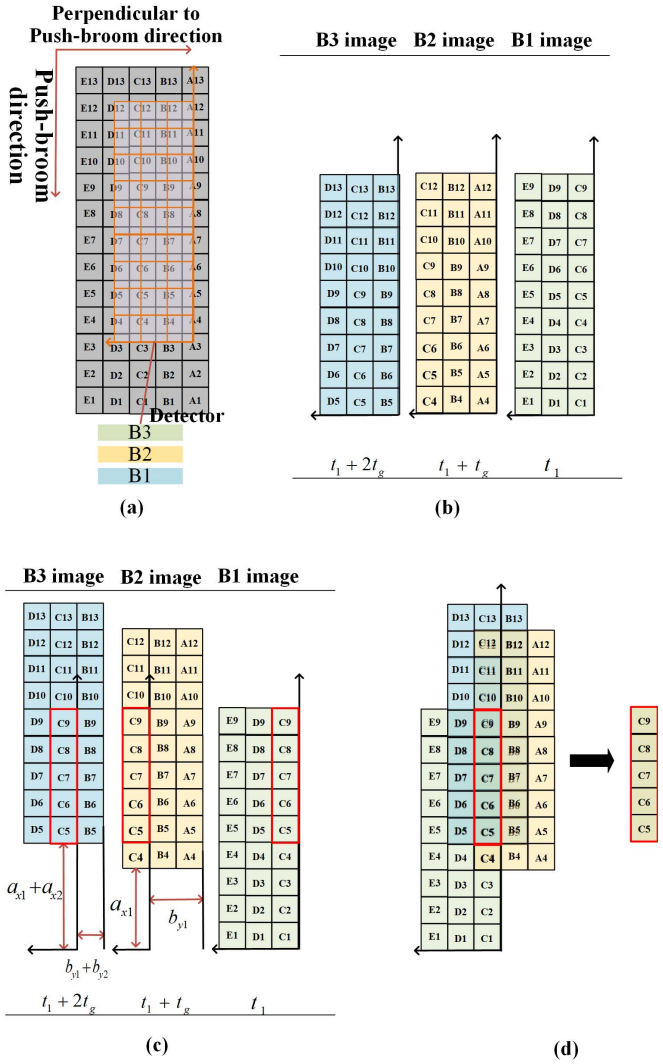

Fig. 8. Fusion process of images taken by bands on each detector: (a) labels of object points and multispectral image acquisition, (b) images of different bands and unified image fusion coordinate systems, (c) aligned images in unified image fusion coordinate systems by image transforming, and (d) fusion of matched images.

As shown in Fig. 8, the spectral images of B1, B2, and B3 are represented by blue, orange, and green, respectively, and the scene point corresponding to each pixel is marked as (A, B), A $\in \{A, B, C, \ldots,\}$, B $\in \{1, 2, 3, \ldots,\}$. As shown in Fig. 8(a), 3 $\times$ 9 pixels of the images are taken as an example to explain the fusion process of multispectral images guided by the VVF. As shown in Fig. 8(b), one vertex of each multispectral image (such as the vertex in the lower right corner) is used as the coordinate origin to establish a unified image fusion coordinate system. The time interval is invariable when two adjacent spectral bands scan the same scene point. It can be found that the imaging positions of the same scene point (A, B) in each spectral band are different due to the time-varying velocity $(v_{pxjk}(t), v_{pyjk}(t))$.

As shown in Fig. 8(c), the image motions (a_{xn}, b_{yn}), which are called misalignment in multispectral images, are calculated by $(v_{pxjk}(t)v_{pyjk}(t))$. a_{xn} represents the misalignment in the push-broom direction. b_{yn} represents the misalignment in the vertical push-broom direction. The image motions between the nth band and the $n+1$th spectral band are

$$a_{xn} = \frac{\int_{t_1+(n-1)t_g}^{t_1+nt_g} v_{pxjk}(t)\,dt}{a}\text{pixels} \tag{37}$$

$$b_{yn} = \frac{\int_{t_1+(n-1)t_g}^{t_1+nt_g} v_{pyjk}(t)\,dt}{a}\text{pixels} \tag{38}$$

$$j = 0, k = 0, n = 1, 2, \ldots, E. \tag{39}$$

E is the total number of spectral bands. Initial imaging time of first band (such as B1 in Fig. 8) is t_1. The adjacent band starts to image the same scene after t_g. The same scene point can be quickly aligned in the unified image fusion coordinate system by transforming the image with (a_{xn}, b_{yn}). The image of the first band (B1) is selected as the benchmark. As shown in Fig. 8(d), the image of the nth band is shifted by $(a_{x1} + a_{x2} + \cdots + a_{x(n-1)}, b_{y1} + b_{y2} + \cdots + b_{y(n-1)})$ pixels in sequence,

Authorized licensed use limited to: Changchun Inst of Optics Fine Mechanics & Physics. Downloaded on February 07,2023 at 01:20:13 UTC from IEEE Xplore. Restrictions apply.

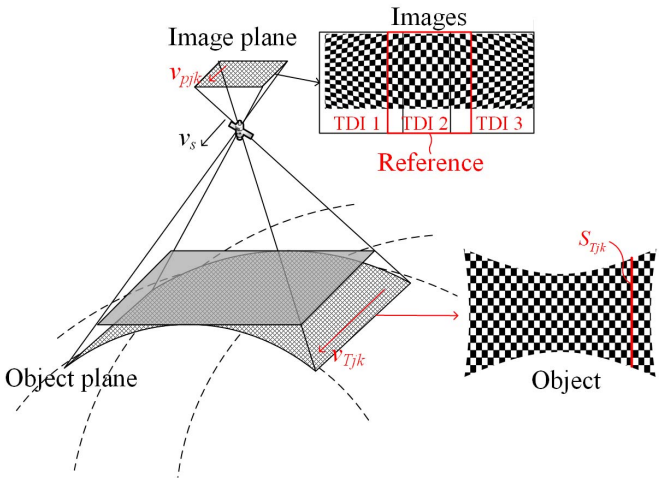

Fig. 9. Distortion that is affected by VVF of image and object areas.

and all spectral images are overlaid in the unified image fusion coordinate system.

When the preprocessing of the fused image is completed under the guidance of image motion, the color image is fused through component substitution.

B. Image Stitching With VVF Model and Line-Point Consistency

The distortion caused by the nonuniform VVF among detectors still exists after the multispectral image fusion. In order to obtain a stitched image with low distortion during the image stitching process, the image with minimum distortion is selected as the reference image according to the relationship between VVF and distortion. Then, images are stitched with distortion correction leveraging line-point consistency based on global and local collinear structures.

The benchmark image that has the smallest distortion is found through the relationship between VVF and distortion, as shown in Fig. 9. $v_{Tjk}(t)$ is the velocity on the object plane

$$v_{Tjk}(t) = \frac{L_{jk}(t) \cdot v_{pjk}}{f}. \tag{40}$$

It can be known from kinematic equation, distance equals velocity times time, that the distance traveled by object points is $S_{Tjk}(t) = v_{Tjk}(t) \cdot \Delta t = v_{pjk} \cdot L_{jk}(t) \cdot \Delta t / f$. Δt is the time for imaging. The focal length of lens f is fixed. Distances $S_{Tjk}(t)$ on the Earth are different because of anisotropic velocities $v_{pjk}(t)$ on the object plane and satellite–object distance $L_{jk}(t)$. Thus, the object plane shrinks in the middle and extends on both sides, as shown in Fig. 9. However, the size and the number of pixels of the detectors remain unchanged. The distortion on the edge of the image is severe after projecting the object plane to the square image plane. The IVVU parameter [see (41)] is defined with the velocity on the image plane, which is proportional to the degree of distortion. The image with the minimum IVVU value is selected as the stitching reference image

$$\text{IVVU} = \sum_{j=1}^{M-1} \sum_{K=1}^{N-1} \left| \arctan\left(v_{pyjk}(t) / v_{pxjk}(t)\right) \right|. \tag{41}$$

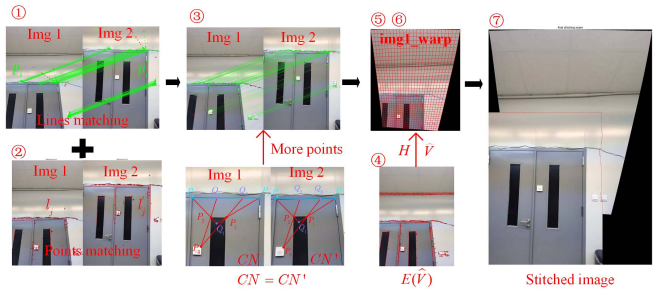

Fig. 10. Image stitching process.

Finally, according to the reference image, the fused images are precisely stitched with the point-line registration method that preserves local lines and global colinear lines.

As shown in Fig. 10, we input img1 and reference img2 that are selected by IVVU as an example to example the stitching process. It is implemented as follows [30].

1) Use the SURF algorithm to search for the matched point pairs $\{p_i, p_i'\}_{i=1,2,\ldots,I}$ of the two images: img1 and img2.
2) Employ the LSD algorithm to obtain feature lines of two images, img1 and img2, and match feature line pairs $\{l_j, l_j'\}_{j=1,2,\ldots,J}$.
3) More matched points and lines are found through the method that the projected invariant feature number CN of two images is equal.
   $\mathcal{P} = \{P_i\}_{i=1,2,\ldots,I+J}$ is a point set including I matched points and J endpoints of the matched lines from steps 1) and 2). The point set $\mathcal{Q} = \{Q_i{}^{(j)}\}_{j=1,2,\ldots,K}$ is the intersection set of any two lines in the line set $\{P_i P_{i+1}\}_{i=1,2,\ldots,I+J}$. $Q_i{}^{(j)}$ can be represented by P_i and P_{i+1} as
   $$Q_i{}^{(j)} = a_i{}^{(j)} P_i + b_i{}^{(j)} P_{i+1}. \tag{42}$$
   The expression for CN is
   $$CN(\mathcal{P}, \mathcal{Q}) = \prod_{i=1}^{I+J} \left(\prod_{j=1}^{K} \frac{a_i^{(j)}}{b_i^{(j)}} \right). \tag{43}$$
4) The RANSAC algorithm is used to refine the matched points and estimate homography H for img1.
5) A mesh grid is constructed in img1, whose index is b, and the vector $\mathbf{V}$ is used to represent the original coordinates of mesh vertices
   $$\mathbf{V} = [x_1, y_1, x_2, y_2, \ldots, x_b, y_b]^T \left(\mathbf{V} \in \mathbb{R}^{2b} \right). \tag{44}$$
6) The energy function $E(\widehat{\mathbf{V}})$ [see (45)] is constructed, and H is optimized with the constraint of lowest $E(\widehat{\mathbf{V}})$. The coordinate $\widehat{\mathbf{V}}$ of the mesh vertices of img1 is calculated by the optimized H. The reference image img2 remains unchanged. The image img1_warp whose distortion is corrected is obtained through mesh transformation
   $$E\left(\widehat{\mathbf{V}}\right) = E_{lp}\left(\widehat{\mathbf{V}}\right) + E_a\left(\widehat{\mathbf{V}}\right) + E_d\left(\widehat{\mathbf{V}}\right) \tag{45}$$
   $$\widehat{\mathbf{V}} = [\widehat{x_1}, \widehat{y_1}, \widehat{x_2}, \widehat{y_2}, \ldots, \widehat{x_b}, \widehat{y_b}]^T \left(\widehat{\mathbf{V}} \in \mathbb{R}^{2b} \right). \tag{46}$$

Authorized licensed use limited to: Changchun Inst of Optics Fine Mechanics & Physics. Downloaded on February 07,2023 at 01:20:13 UTC from IEEE Xplore. Restrictions apply.

In this formula, $E_{lp}(\widehat{\mathbf{V}})$ solves the preservation problem of the linear structure. There is $E_{lp}(\hat{V}) = \lambda_{lo}E_{lo}(\hat{V}) + \lambda_{gl}E_{gl}(\hat{V})$, in which $E_{lo}(\hat{V})$ and $E_{gl}(\hat{V})$ are constraints on local lines and global colinear line segments, respectively. λ_{lo} and λ_{gl} are the weights of each term. $E_a(\widehat{V})$ controls the matched point pairs and line pairs. $E_d(\widehat{V})$ controls the distortion during stitching by maintaining the slope of the grid lines and the uniformity of adjacent grids.

7) Select the two boundary lines of the overlapping area of img2 and img1_wrap. Those two boundary lines are used as sink and source, respectively. The best fusion boundary is found by the graph-cut algorithm [31]. Finally, the stitching is completed.

IV. Experiment

The high-fidelity field experiment is designed to demonstrate the feasibility of the above method. The turntable drives the camera to simulate the attitude maneuver of the agile satellite. Lens and detectors are used to simulate the camera of the agile satellite. The design and results of the field experiment are introduced as follows.

A. Experiment Design

The rotation speed of the turntable and the installation angle of the detector involved in the field experiment are first calculated by an application scenario of the agile satellite. It should be noted that the influence of image flutter, which is caused by the flywheel of the agile satellite, is ignored. The satellite attitude varies linearly with time to simplify experimental operation.

A Sun-synchronous satellite with a 500-km orbit height is used to accomplish agile imaging along the "west-to-east" track of electricity transmission from Hami to Zhengzhou. The orbital inclination angle is 97°, the semimajor axis of this orbit is 6878.14 km, the RAAN is 295°, the argument of perigee is 0°, and the eccentricity of this orbit is 0. The epoch time is 4:00:00 on July 12, 2021, and the Greenwich sidereal time at this epoch time is 6.11 rad.

The velocities on the image plane that is spliced with three detectors are calculated. The image of each detector has 4120 × 4120 pixels. The focal length of the lens is 3.5 m. The trajectory of scanning on the Earth is shown in Fig. 11(a), and the adjustment of satellite attitude is shown in Fig. 11(b). The resultant velocities on the image plane at 2241 s are shown in Fig. 11(c).

Fig. 11(d) shows the distribution of the drift angles at time 2241 s on the image plane. The value of the resultant velocity at the center of image plane is $\upsilon_p = 0.062$ m/s, and its drift angle is $\xi_p = -1.033°$, which has considered Earth's Rotation, curvature of Earth, and satellite attitudes. In the field experiment, the cooperation of the detector installation angle $\xi_p = -1.033°$ and the rotation speed of the turntable $\upsilon_p = 0.062$ m/s are employed to substitute the resultant velocity.

The installation angle of one of the detectors is equal to the drift angle ξ_p. As shown in Fig. 12(a), TDI CMOS-2 is installed on the YOZ plane, which receives the image reflected

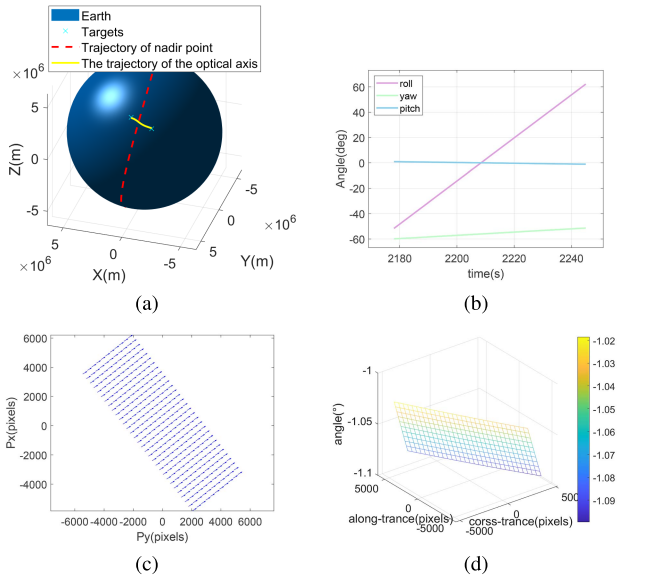

Fig. 11. Simulation: (a) trajectory of scanning on the Earth, (b) adjustment of satellite attitude, (c) VVF on the image plane at 2241 s, and (d) drift angle at 2241 s on the image plane.

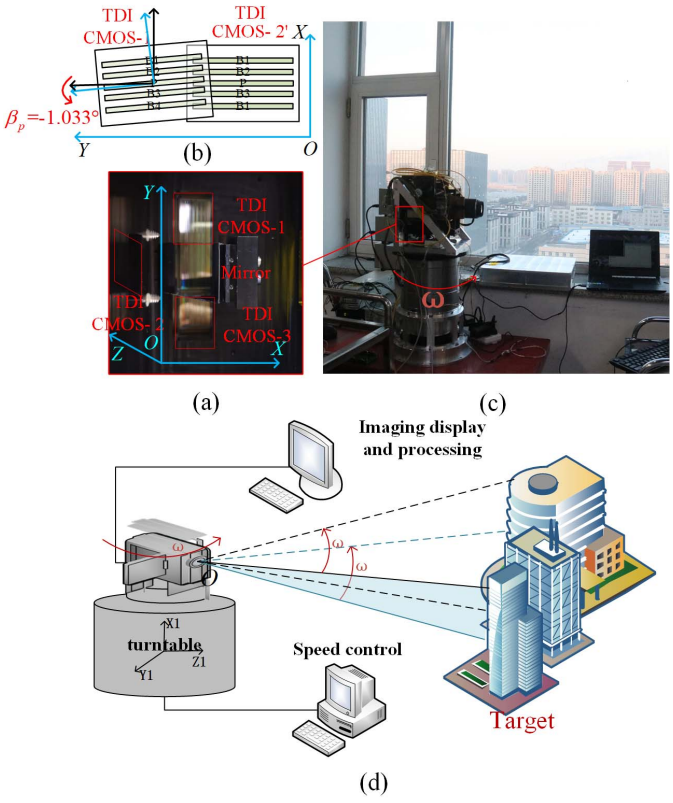

Fig. 12. Field experiments: (a) theory of field experiment, (b) devices of field experiment, (c) XOY plane of detector, and (d) arrangement of detectors.

by a 45° prism. TDI CMOS-1 is installed on the XOY plane and rotates with $\xi_p = -1.033°$ around its central axis, which is perpendicular to the XOY plane. $\xi_p = -1.033°$ is the tilt angle between the equivalent mirror detectors TDI CMOS-2' and TDI CMOS-1 on the XOY plane, which is clearly illustrated in Fig. 12(b). In the push-broom direction of the image plane, multispectral bands, B1, B2, and B3, are corresponding to

Authorized licensed use limited to: Changchun Inst of Optics Fine Mechanics & Physics. Downloaded on February 07,2023 at 01:20:13 UTC from IEEE Xplore. Restrictions apply.

blue, green, and red channels. The width of each spectral band is $S_p = 0.672$ mm, and the interval among spectral bands is $S_h = 2$mm.

In the field experiment, the camera does circular rotation instead of linear motion to acquire the effect of imaging the spherical Earth by satellite. There are differences in distances between cameras and buildings during rotary scanning, which is equivalent to the differences in distances between satellites and targets caused by the spherical curvature of the Earth. The rotation speed of the turntable is used to generate the value of resultant velocity v_p on the image plane. The field experiment uses those special arranged detectors, a 1-D turntable, and an optical lens to scan buildings. Devices and process of this field experiment are shown in Fig. 12(a) and (b). The XOY plane of the detector is placed on the focal plane of the lens, the detectors and lens are fixed on the turntable, and the optical axis of the lens is parallel with the $Z1$-axis of the turntable. The focal length of the lens is 200 mm. The time frequency of detectors is 9 kHz. Turntable with a constant speed of $18\circ/s$ drives the detectors and the lens rotating around the $X1$-axis to ensure that the velocity of the image plane is $v_p = 0.062$ m/s.

B. Field Experiment Results

The original images acquired by the TDI CMOS-1 and TDI CMOS-2 are shown in Fig. 13(a), (c), (e), (g), (i), and (k), in which the images of TDI CMOS-2 have been mirror-flipped. The size of each original image is 1413 pixels $\times$ 1024 pixels. There is obvious misalignment among those images. The value of misalignment among images can be calculated by integrating velocities with time. The integration time between two adjacent bands is $t_h = 0.0424$ s. The velocity components v_x along the push-broom direction and v_y, which is perpendicular to the push-broom direction, are expressed as follows:

$$v_{xpjk} = v_p \cos\left(\xi_p\right) \tag{47}$$

$$v_{ypjk} = v_p \sin\left(\xi_p\right). \tag{48}$$

The misalignment is calculated by substituting (47) and (48) into (37)–(39), whose results are shown in Table I. The accuracy of misalignment calculation is evaluated based on the traditional SURT algorithm. The average values of the misalignments acquired by the SURF algorithm are also shown in Table I. It can be found that the difference between misalignments calculated by our method and the SURF algorithm remains one pixel.

Meanwhile, aiming at the time during the process of calculating TDI CMOS-1 images with different methods, time in the VVF model is 13.19% of the SURF algorithm between B1 and B2 images, and time in the VVF model is 12.24% of the SURF algorithm between B2 and B3 images.

For images of TDI COMS2, time in the VVF model is only 6.94% of the SURF algorithm between B1 image and B2 image, and time in the VVF model is only 6.55% of the SURF algorithm between B2 and B3 images. It can be found that our method is faster and has similar precision.

Next, misalignments calculated by the VVF model in Table I are used to align multispectral images. The images

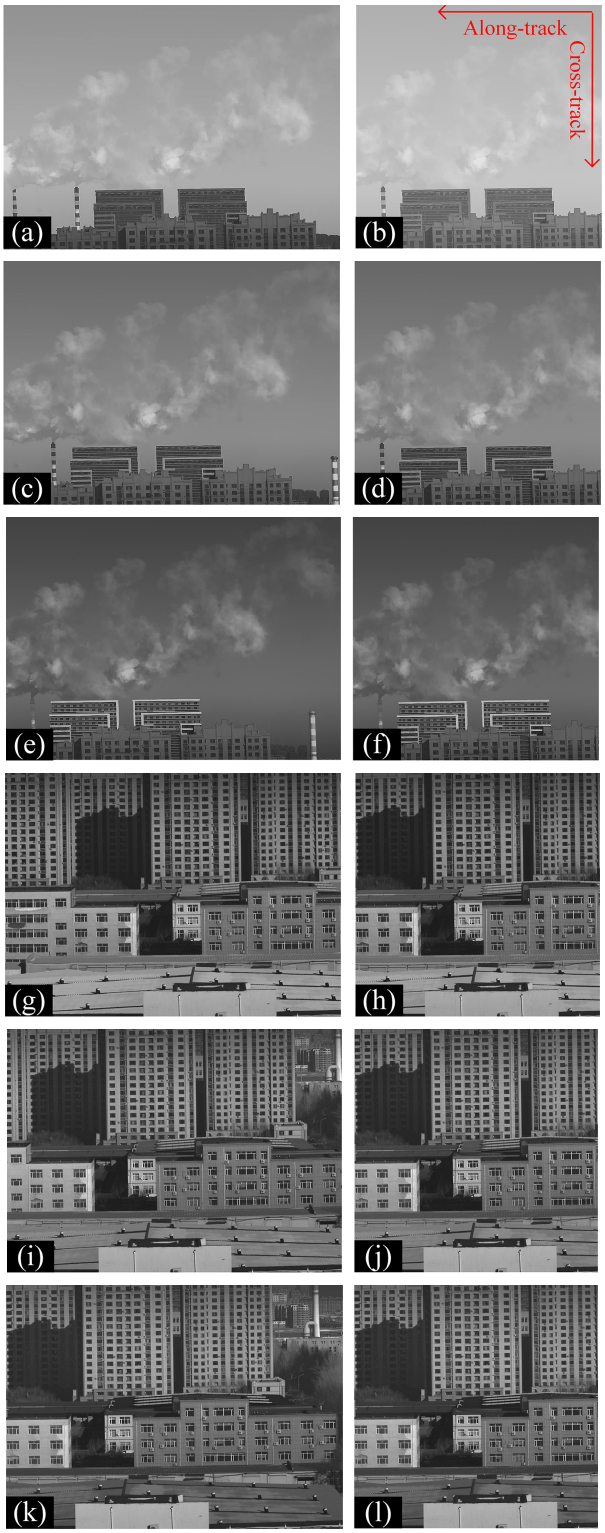

Fig. 13. Multispectral images: (a) original image (TDI CMOS-1, B1), (b) matched image (TDI CMOS-1, B1), (c) original image (TDI CMOS-1, B2), (d) matched image (TDI CMOS-1, B2), (e) original image (TDI CMOS-1, B3), (f) matched image (TDI CMOS-1, B3), (g) original image (TDI CMOS-2, B1), (h) matched image (TDI CMOS-2, B1), (i) original image (TDI CMOS-2, B2), (j) matched image (TDI CMOS-2, B2), (k) original image (TDI CMOS-2, B3), and (l) matched image (TDI CMOS-2, B3).

(see Fig. 13(b)-B1, (d)-B2, and (f)-B3) are aligned images from the original images (see Fig. 13(a), (c), and (e)) of TDI CMOS-1 by misalignment. Blue, green, and red channels are

Authorized licensed use limited to: Changchun Inst of Optics Fine Mechanics & Physics. Downloaded on February 07,2023 at 01:20:13 UTC from IEEE Xplore. Restrictions apply.

TABLE I
MISALIGNMENT CALCULATED BY THE VVF MODEL AND THE SURF ALGORITHM

Detector	VVF model TDI CMOS-1		VVF model TDI CMOS-2		SURF TDI CMOS-1		SURF TDI CMOS-2	
Band	B2-B1	B3-B2	B2-B1	B3-B2	B2-B1	B3-B2	B2-B1	B3-B2
Along-track/pixels	-97.414	-194.827	-97.429	-194.857	-98.806	-194.190	-96.286	-193.668
Cross-track /pixels	-1.220	-2.941	0.500	1.000	-1.250	-2.546	0.509	0.882
Time/s	1.589	1.589	1.589	1.589	12.047	12.984	22.891	24.250

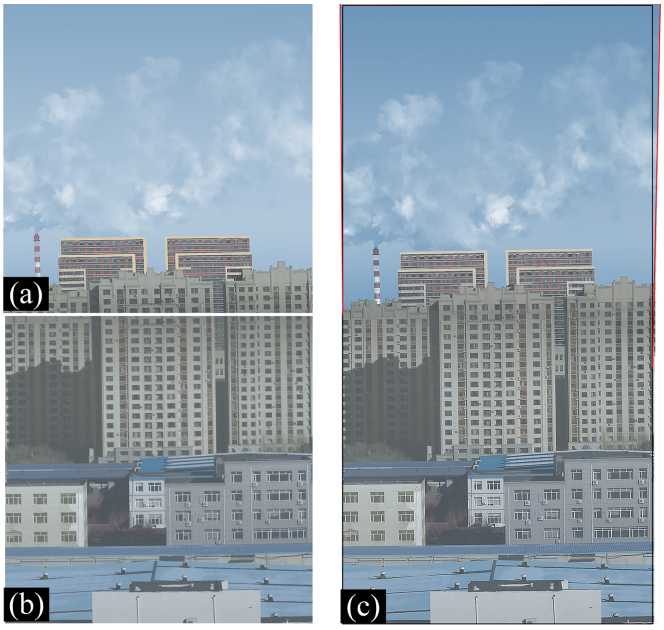

Fig. 14. Color images: (a) fused image of TDI CMOS-1, (b) fused image of TDI CMOS-2, and (c) stitched image.

filled with images of B1, B2, and B3, respectively, to obtain the color images that are shown in Fig. 14. The process of image fusion of TDI CMOS-2 is the same as TDI CMOS-1. The size of Fig. 14(a), the image of TDI CMOS-1, is 1024 $\times$ 1016 pixels. The size of Fig. 14(b), the image of TDI CMOS-2, is 1024 $\times$ 1022 pixels.

Then, the fused images are stitched together. We substitute (47) and (48) into (41) to calculate IVVU. The values of IVVU of TDI CMOS-1 and TDI CMOS-2 are 3.781×10^4 and 0, respectively. The image of TDI CMOS-2 that has the smaller IVVU is selected as the reference. The two images [see Fig. 14(a) and (b)] are stitched using the method described in Section III. Finally, the stitched image with a size of 1051 $\times$ 2032 pixels is generated, as shown in Fig. 14(c). The part outlined by the black line represents the size of the image without distortion correction. The red outline draws the edge of the distortion-corrected image. It can be found that the corrected image expands at the edge of the stitched image, which accords with the distortion correction characteristics of remote sensing satellite images.

A quantitative comparison is made among the results of our image stitching method, SURF, SIFT, and SPW algorithms.

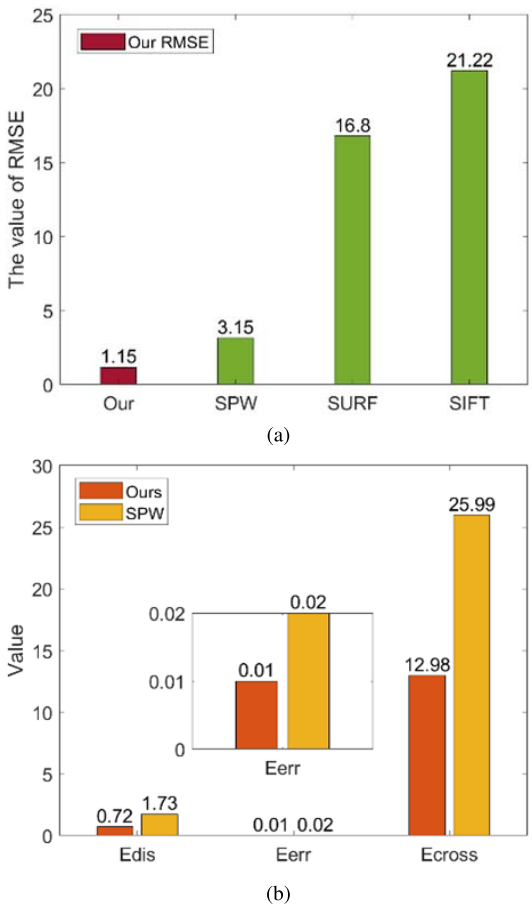

Fig. 15. Quantitative analysis of image stitching accuracy: (a) RMSE values of the algorithm, the SURF algorithm, the SIFT algorithm, and the SPW algorithm, and (b) quantitative comparison on linear structure preservation between the SPW algorithm and algorithm.

The root mean square error (RMSE), the collinearity of points E_{err}, the distance of matched lines E_{dis}, and the discrepancy in the direction of matched lines E_{cross}, which are introduced in ref. [30], are the comparison indexes.

Fig. 15(a) shows the histogram of the RMSE values of the four algorithms. The x-coordinate shows the names of methods. The y-coordinate represents the value of RMSE. The RMSE of our method is the smallest, an order of magnitude smaller than SITF and SURF, and 63% lower than that value of SPW.

Furthermore, the evaluation metrics in [30] are used to evaluate the linear structure. Fig. 15(b) shows the

Authorized licensed use limited to: Changchun Inst of Optics Fine Mechanics & Physics. Downloaded on February 07,2023 at 01:20:13 UTC from IEEE Xplore. Restrictions apply.

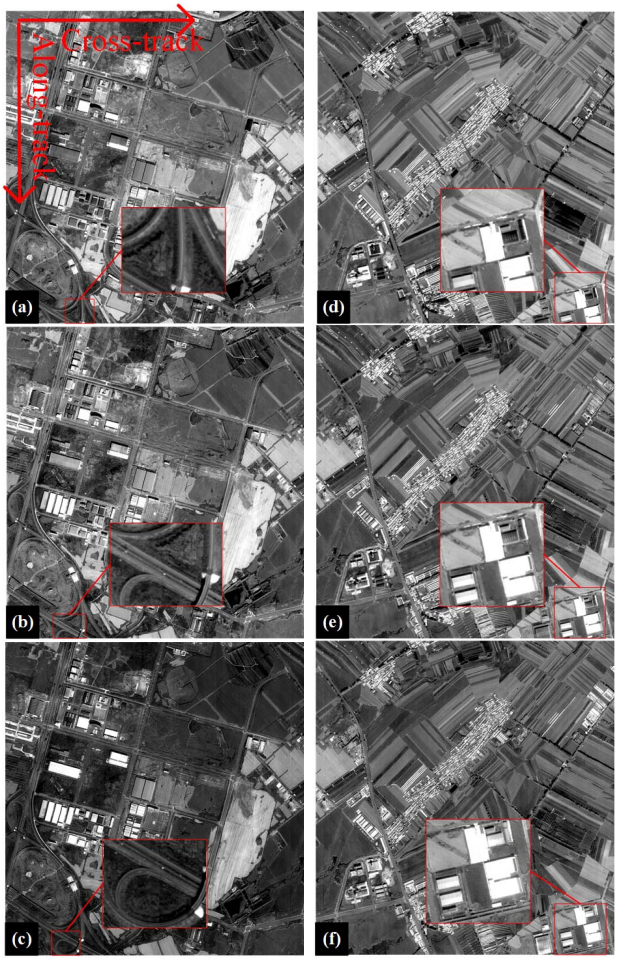

Fig. 16. Multispectral images on each detector of agile satellite: (a) Detector 1, B1; (b) Detector 1, B1; (c) Detector 1, B2; (d) Detector 1, B2; (e) Detector 1, B3; and (f) Detector 1, B3.

histogram of E_{err}, E_{dis}, and E_{cross} of our method and SPW. The x-coordinate shows the evaluation metrics, and the y-coordinate represents the value. Our E_{dis} is 40% of that of SPW [28]. Our E_{err} is 0.01 and E_{cross} is 12.98, which are only 50% of those of SPW. It can be found that each evaluation metric of ours outperforms those of other methods.

V. Fusion and Stitching for Images of Agile Satellite

Our proposed method is used to fuse and stitch a set of image data acquired by an agile satellite JL-1. The orbit altitude is 656 km. The maximum angular velocity for the attitude maneuver is 5°/s, and the maximum attitude angle is 20°. The image plane of JL-1 is stitched with four detectors. Images taken by Detector 1, in the middle of the image plane, and adjacent Detector 2, at the edge of the image plane, are shown in Fig. 16. B1, B2, and B3 are the red band, the green band, and the blue band of each detector, respectively.

Fig. 16, respectively, shows the multispectral images of B1, B2, and B3 of two detectors when agile satellite images Jilin, China. The reference object of each detector is marked with a red frame to demonstrate a mismatch in the original images. Among images of Detector 1, there is no overpass in the image of B1, half overpass in the image of B2, and a whole overpass in the image of B3. It is the same situation in Detector 2 that those five houses become more and more complete from images of B1 and B2.

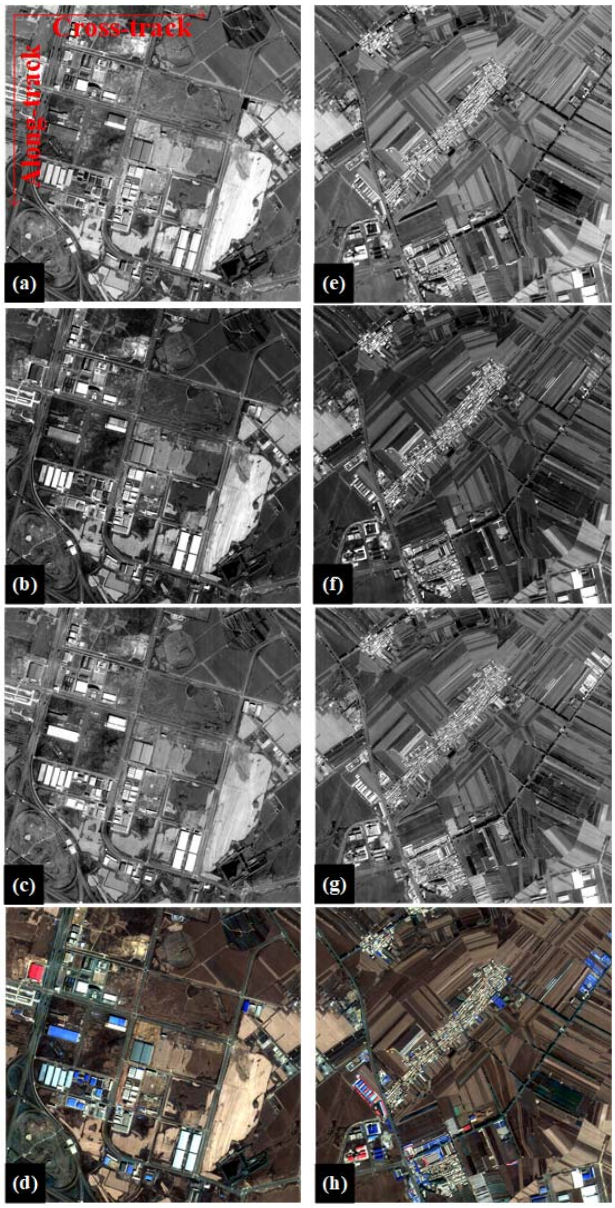

Fig. 17. Aligned images and fused images of three bands on each detector of agile satellite: (a) aligned image of B1, Detector 1; (b) aligned of image B2, Detector 1; (c) aligned of image B3, Detector 1; (d) fused image of Detector 1; (e) aligned image of B1, Detector 2; (f) aligned image of B2, Detector 2; (g) aligned image of B3, Detector 2; and (h) fused image of Detector 2.

The fusion results are shown as follows. The registered images are shown in Fig. 17(a)–(c), which are the multispectral images of three bands of the first detector, and Fig. 17(e)–(g) shows the multispectral images of three bands of the second detector. The color images after fusion are shown in Fig. 17(d) and (h). There are no artifacts for fused images caused by mismatches. It only takes 2.5522 s to calculate misalignments by the VVF model.

The color image of Detector 1 is selected as the benchmark. Fig.18 shows the stitched image. It also expands at the edge of the stitched image (the part outlined by the green line

Authorized licensed use limited to: Changchun Inst of Optics Fine Mechanics & Physics. Downloaded on February 07,2023 at 01:20:13 UTC from IEEE Xplore. Restrictions apply.

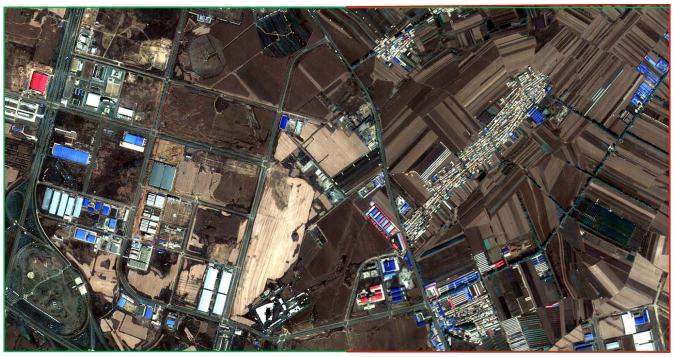

Fig. 18. Stitched image.

represents the size of the image without distortion correction; the red outline draws the edge of the distortion-corrected image). RMSE is 1.04. E_{dis}, E_{err}, and E_{cross} are 0.83, 0.02, and 37.06, respectively. It can be found that our proposed method is fully applicable to the images of the in-orbit agile satellite.

VI. Conclusion

In this article, an image fusion and stitching method with the VVF model and the line-point registration algorithm is proposed to realize fast spectral fusion and preserve the local and global structures of the image. The field and on-orbit experiments are designed to demonstrate the feasibility of applying this method to fuse and stitch images that are taken by agile satellite detectors. The following conclusions are drawn based on the results and the experiments.

1) Due to the misalignment and distortion of agile satellite images, the fusion of interband images is slower, and the stitching accuracy of interdetector images is poorer.
2) The image fusion method uses the VVF model considering the satellite attitude and the Earth's rotation to calculate the misalignment among the images of bands in each detector. Our method is faster while ensuring registration accuracy. Meanwhile, the difference between the values of misalignment, calculated by the VVF model and the traditional image registration algorithm, is less than 1 pixel.
3) Based on the reference image selected by IVVU, the image stitching uses line-point consistency and linear structures to correct distortion at the same time. It can be proved that our method has a higher stitching accuracy.
4) In-orbit images can be fast fused and accurately stitched, which proves the feasibility and superiority of this method.

Our method provides a theoretical basis for the fast processing of multispectral images. It not only has theoretical significance but also has practical significance. This article gives a model for improving image processing speed and quality, which is a direction for future research.

References

[1] L. Jiang and X. Yang, "Study on enlarging the searching scope of staring area and tracking imaging of dynamic targets by optical satellites," *IEEE Sensors J.*, vol. 21, no. 4, pp. 5349–5358, Feb. 2021.

[2] W. Li, C. Hu, L. Zhang, and C. Yan, "Drift angle compensation method for a high-resolution and wide-range space camera," *Measurement*, vol. 158, Jul. 2020, Art. no. 107710.

[3] W. Qiu and C. Xu, "Attitude maneuver planning of agile satellites for time delay integration imaging," *J. Guid., Control, Dyn.*, vol. 43, no. 1, pp. 46–59, Jan. 2020.

[4] D. Wu, Y. Chen, Q. Li, Z. Xu, H. Feng, and Y. Man, "Attitude scheduling and verification for dynamic imaging of agile satellites," *Optik*, vol. 206, Mar. 2020, Art. no. 164365.

[5] C. Xu et al., "Study of space optical dynamic push-broom imaging along the trace of targets," *Optik*, vol. 202, Feb. 2020, Art. no. 163640.

[6] M. Bagnardi, P. J. González, and A. Hooper, "High-resolution digital elevation model from tri-stereo Pleiades-1 satellite imagery for lava flow volume estimates at Fogo Volcano," *Geophys. Res. Lett.*, vol. 43, no. 12, pp. 6267–6275, Jun. 2016.

[7] R. Pu, S. Landry, and Q. Yu, "Assessing the potential of multi-seasonal high resolution Pleiades satellite imagery for mapping urban tree species," *Int. J. Appl. Earth Observ. Geoinf.*, vol. 71, pp. 144–158, Sep. 2018.

[8] X. Tang, F. Hu, M. Wang, J. Pan, S. Jin, and G. Lu, "Inner FoV stitching of spaceborne TDI CCD images based on sensor geometry and projection plane in object space," *Remote Sens.*, vol. 6, no. 7, pp. 6386–6406, Jul. 2014.

[9] W. A. Wahballah, F. Eltohamy, and T. M. Bazan, "Influence of attitude parameters on image quality of very high-resolution satellite telescopes," *IEEE Trans. Aerosp. Electron. Syst.*, vol. 57, no. 2, pp. 1177–1183, Apr. 2021.

[10] P.-L. Lu, Y.-C. Li, L.-X. Jin, and G.-N. Li "Image motion velocity field model of space camera with large field and analysis on three-axis attitude stability of satellite," *Opt. Precis. Eng.*, vol. 24, no. 9, pp. 2173–2182, Sep. 2016.

[11] J. Wang, P. Yu, C. Yan, J. Ren, and B. He, "Space optical remote sensor image motion velocity vector computational modeling," *Acta Optica Sinica*, vol. 24, no. 12, pp. 1585–1589, 2004.

[12] Y. Teshima and A. Iwasaki, "Correction of attitude fluctuation of Terra spacecraft using ASTER/SWIR imagery with parallax observation," *IEEE Trans. Geosci. Remote Sens.*, vol. 46, no. 1, pp. 222–227, Jan. 2008.

[13] L. Jiang, X. Yang, Y. Wang, and C. Su, "Matching design about pixel number of interleaving assembly time delay integration CCD for lateral swing imaging," *Laser Optoelectronics Prog.*, vol. 53, no. 5, pp. 5110401–5110409, 2016.

[14] T. Xu, X. Yang, S. Wang, J. Han, L. Chang, and W. Yue, "Imaging velocity fields analysis of space camera for dynamic circular scanning," *IEEE Access*, vol. 8, pp. 191574–191585, 2020.

[15] J. Han et al., "Image motion of remote sensing camera with wide field of view over the Antarctic and Arctic," *IEEE J. Sel. Topics Appl. Earth Observ. Remote Sens.*, vol. 14, pp. 3475–3484, 2021.

[16] X. Tong et al., "Attitude oscillation detection of the ZY-3 satellite by using multispectral parallax images," *IEEE Trans. Geosci. Remote Sens.*, vol. 53, no. 6, pp. 3522–3534, Jun. 2015.

[17] H. Simon, R. Michael, H. Tobias, S. Oliver, and O. Wolfgang, "Multi-positional image-based vibration measurement by holographic image replication," *Light, Adv. Manuf.*, vol. 2, p. 425, Dec. 2021.

[18] R. Perrier, E. Arnaud, P. Sturm, and M. Ortner, "Estimation of an observation satellite's attitude using multimodal pushbroom cameras," *IEEE Trans. Pattern Anal. Mach. Intell.*, vol. 37, no. 5, pp. 987–1000, May 2015.

[19] S. Wang, X. Yang, T. Xu, J. Han, L. Chang, and W. Yue, "Instantaneous image-rotation analysis for dynamic format imaging of space CMOS camera," *Acta Optica Sinica*, vol. 40, no. 21, 2020, Art. no. 2111003.

[20] S. J. Liu et al., "Geometric modeling of attitude jitter for three-line-array imaging satellites," *Opt. Exp.*, vol. 29, no. 13, pp. 20952–20969, 2021.

[21] D. G. Lowe, "Distinctive image features from scale-invariant keypoints," *Int. J. Comput. Vis.*, vol. 60, no. 2, pp. 91–110, 2004.

[22] H. Bay, A. Ess, T. Tuytelaars, and L. Van Gool, "Speeded-up robust features (SURF)," *Comput. Vis. Image Understand.*, vol. 110, no. 3, pp. 346–359, 2008.

[23] J. Chen and J. Tian, "Real-time multi-modal rigid registration based on a novel symmetric-SIFT descriptor," *Prog. Natural Sci.*, vol. 19, no. 5, pp. 643–651, May 2009.

[24] J. Chen, J. Tian, N. Lee, J. Zheng, R. T. Smith, and A. F. Laine, "A partial intensity invariant feature descriptor for multimodal retinal image registration," *IEEE Trans. Biomed. Eng.*, vol. 57, no. 7, pp. 1707–1718, Jul. 2010.

[25] L. Huang, T. Sun, T. Zhang, and H. You, "Application of DIROEF algorithm for noncollinear multiple CCD array stitching of the Chinese mapping satellite 1–02," *IEEE Geosci. Remote Sens. Lett.*, vol. 14, no. 4, pp. 519–523, Apr. 2017.

Authorized licensed use limited to: Changchun Inst of Optics Fine Mechanics & Physics. Downloaded on February 07,2023 at 01:20:13 UTC from IEEE Xplore. Restrictions apply.

[26] R. G. von Gioi, J. Jakubowicz, J.-M. Morel, and G. Randall, "LSD: A fast line segment detector with a false detection control," *IEEE Trans. Pattern Anal. Mach. Intell.*, vol. 32, no. 4, pp. 722–732, Apr. 2010.
[27] T. Wang et al., "A spliced satellite optical camera geometric calibration method based on inter-chip geometry constraints," *Remote Sens.*, vol. 13, no. 14, p. 2832, Jul. 2021.
[28] C. Xu, G. Jin, X. Yang, T. Xu, and L. Chang, "Inversion restoring algorithm for whiskbroom scanning images synthesized with deep convolutional neural network," *Acta Optica Sinica*, vol. 39, no. 12, 2019, Art. no. 1228001.
[29] T. Liao and N. Li, "Single-perspective warps in natural image stitching," *IEEE Trans. Image Process.*, vol. 29, pp. 724–735, 2020.
[30] Q. Jia et al., "Leveraging line-point consistence to preserve structures for wide parallax image stitching," in *Proc. IEEE/CVF Conf. Comput. Vis. Pattern Recognit. (CVPR)*, Jun. 2021, pp. 12181–12190.
[31] Y. Boykov and V. Kolmogorov, "An experimental comparison of min-cut/max-flow algorithms for energy minimization in vision," *IEEE Trans. Pattern Anal. Mach. Intell.*, vol. 26, no. 9, pp. 1124–1137, Sep. 2004.

Jiamin Du received the B.S. degree in physics from Nankai University, Tianjin, China, in 2020. She is currently pursuing the Ph.D. degree in optical engineering with the Changchun Institute of Optics, Fine Mechanics and Physics, Chinese Academy of Sciences, Changchun, China, the University of Chinese Academy of Sciences, Beijing, China, and the Key Laboratory of Space-Based Dynamic & Rapid Optical Imaging Technology, Chinese Academy of Sciences, Changchun, Jilin, China.

Her research interests include optical design and dynamic optical remote sensing imaging.

Xiubin Yang was born in Jilin, China, in 1982. He received the B.S. degree in physics from Nankai University, Tianjin, China, in 2006, and the Ph.D. degree in optical engineering from the Chinese Academy of Sciences, Changchun, China, in 2011.

From 2013 to 2020, he was an Associate Professor with the Key Laboratory of Space-Based Dynamic & Rapid Optical Imaging Technology, Chinese Academy of Sciences. Since 2021, he has been a Professor with the Space New Technique Department, Changchun Institute of Optics, Fine Mechanics and Physics, Chinese Academy of Sciences. He is the author of two books, 32 articles, and 36 inventions. His research interests include the dynamic imaging process of space optical cameras, the new mode of optical imaging, and advanced optical payload technology.

Dr. Yang was a recipient of the Second Prize of China National Science and Technology Progress Award in 2017, the First Prize of Provincial Science and Technology Progress Award in 2014, and the Seventh Outstanding Contribution Award of Changchun city in 2018.

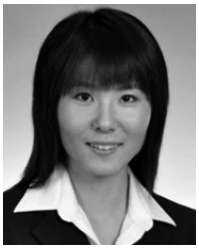

Meili Zhou received the B.S. and M.S. degrees from the School of Electrical Engineering, Beijing Jiaotong University, Beijing, China, in 2009 and 2011, respectively.

She is currently an Assistant Professor with the Department of Space New Technique, Changchun Institute of Optics, Fine Mechanics and Physics, Chinese Academy of Sciences, Changchun, China. Her research interests include electronic Integration technology.

Ziming Tu received the B.E. degree in optical science and engineering from Zhejiang University, Hangzhou, Zhejiang, China, in 2021. He is currently pursuing the M.S. degree in optical engineering with the Changchun Institute of Optics, Fine Mechanics and Physics, Chinese Academy of Sciences, Changchun, China, the University of Chinese Academy of Sciences, Beijing, China, and the Key Laboratory of Space-Based Dynamic & Rapid Optical Imaging Technology, Chinese Academy of Sciences, Changchun, Jilin, China.

His research interests include deep learning, optical remote sensing imaging, and geometric correction.

Shaoen Wang received the B.S. degree from the Harbin Institute of Technology, Weihai, China, in 2019. He is currently pursuing the Ph.D. degree in optical engineering with the Changchun Institute of Optics, Fine Mechanics, and Physics, Chinese Academy of Sciences, Changchun, China, the University of Chinese Academy of Sciences, Beijing, China, the Key Laboratory of Space-Based Dynamic & Rapid Optical Imaging Technology, Chinese Academy of Sciences, Changchun, Jilin, China.

His research interests include dynamic imaging and image processing.

Xingyu Tang received the B.S. degree in information engineering from South China Normal University, Guangzhou, China, in 2022. He is currently pursuing the M.S. degree in optical engineering with the Changchun Institute of Optics, Fine Mechanics and Physics, Chinese Academy of Sciences, Changchun, China, the University of Chinese Academy of Sciences, Beijing, China, and the Key Laboratory of Space-Based Dynamic & Rapid Optical Imaging Technology, Chinese Academy of Sciences, Changchun, Jilin, China.

His research interest is advanced remote sensing techniques.

Lijie Cao is currently studying at the Academy of Remote Sensing, Wuhan University, Wuhan, China.

His research interest is remote sensing instruments.

Xindong Zhao is currently pursuing the B.E. degree in remote sensing with Wuhan University, Wuhan, China, in 2022. He will work toward the M.E. degree in optical engineering at the Changchun Institute of Optics, Fine Mechanics and Physics, Chinese Academy of Sciences, Changchun, China.

His research interests include optical design and remote sensing imaging.

Authorized licensed use limited to: Changchun Inst of Optics Fine Mechanics & Physics. Downloaded on February 07,2023 at 01:20:13 UTC from IEEE Xplore. Restrictions apply.